In situ study of the formation mechanism of two-dimensional superlattices from PbSe nanocrystals

Geuchies, Jaco J.; Van Overbeek, Carlo; Evers, Wiel H.; Goris, Bart; De Backer, Annick; Gantapara, Anjan P.; Rabouw, Freddy T.; Hilhorst, Jan; Peters, Joep L.; Konovalov, Oleg

DOI
10.1038/nmat4746

Publication date
2016

Document Version
Accepted author manuscript

Published in
Nature Materials

Citation (APA)
Geuchies, J. J., Van Overbeek, C., Evers, W. H., Goris, B., De Backer, A., Gantapara, A. P., Rabouw, F. T., Hilhorst, J., Peters, J. L., Konovalov, O., Petukhov, A. V., Dijkstra, M., Siebbeles, L. D. A., Van Aert, S., Bals, S., & Vanmaekelbergh, D. (2016). In situ study of the formation mechanism of two-dimensional superlattices from PbSe nanocrystals. *Nature Materials*, *15*(12), 1248-1254. https://doi.org/10.1038/nmat4746

Supplementary Information for

In-situ study of the formation mechanism of two-dimensional superlattices from PbSe nanocrystals

Jaco J. Geuchies[1,5a†], Carlo van Overbeek[1†], Wiel H. Evers[2,3], Bart Goris[4], Annick de Backer[4], Anjan P. Gantapara[6], Freddy. T. Rabouw[1], Jan Hilhorst[5b], Joep L. Peters[1], Oleg Konovalov[5a], Andrei V. Petukhov[7,8], Marjolein Dijkstra[6], Laurens D.A. Siebbeles[2], Sandra van Aert[4], Sara Bals[4] and Daniel Vanmaekelbergh[1*]

*Corresponding author. E-mail: d.vanmaekelbergh@uu.nl

This supplement contains:

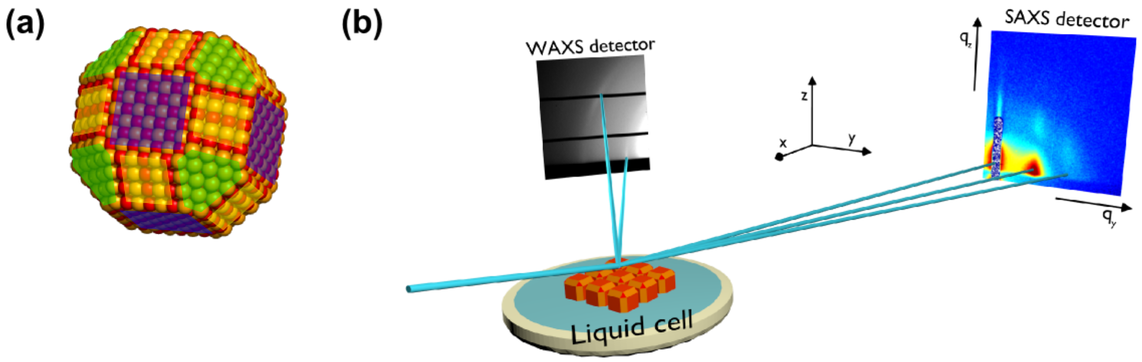

Figure S1: Schematic of the in-situ GISAXS/GIWAXS study of nanocrystal assembly at the liquid/air interface. (a) An atomic model of the PbSe truncated nanocubes, showing the different facets of the NC. Blue indicates the {100} facets, yellow the {110} facets and green the {111} facets. **(b)** Schematic of the setup used for in-situ GISAXS/WAXS experiments. A dispersion of NCs in toluene evaporates in a liquid sample cell. We examine the process of assembly and attachment using grazing-incidence x-ray scattering, by simultaneously monitoring the atomic order on the wide-angle detector and nanoscale order on the small-angle detector.

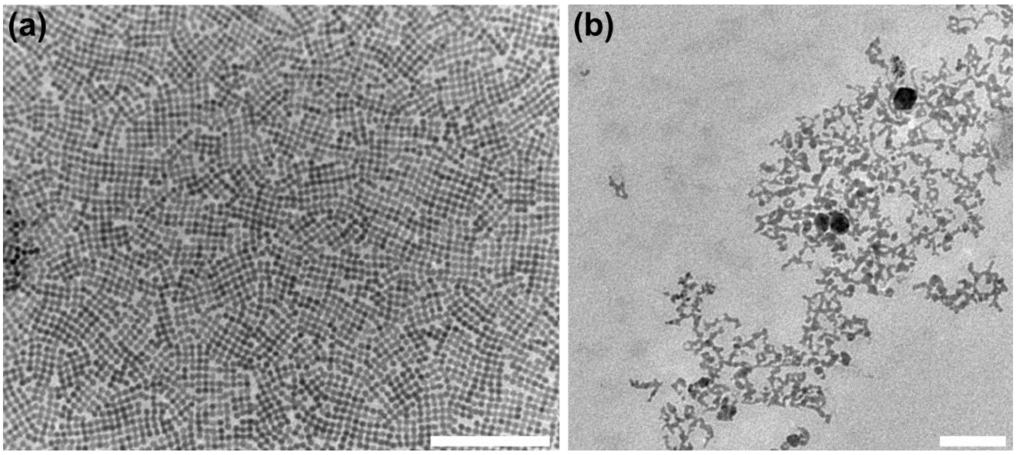

Figure S2: Diffusion limited attachment of PbSe NCs results in structures with no long-range nanoperiodic nor atomic order. (a) Sample where a large amount of simultaneous nucleation has taken place resulting in small domains with square geometry. **(b)** Sintered structures, with no long-range nanoperiodic or atomic order. Scale bars equal 100 nm.

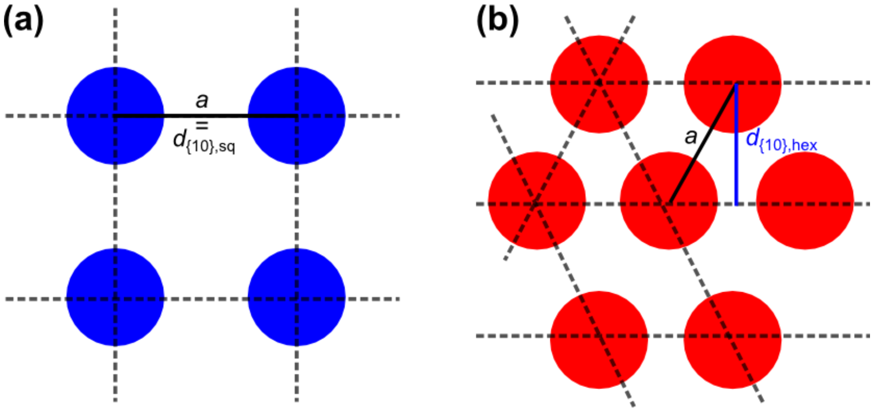

Figure S3: Origin of the first diffraction rod in GISAXS and its relationship to the NC-NC distance. (a) In the case of square ordered superlattices, the NC-NC distance a is equal to the d-spacing of the first lattice plane $\mathrm{d}_{\{10\},\mathrm{sq}}$. The corresponding q-vector is $q_{\{10\},\mathrm{sq}} = 2\pi/d_{\{10\},\mathrm{sq}} = 2\pi/a$. **(b)** For an hexagonal monolayer of NCs, the lattice spacing is not equal to the NC-NC distance; $d_{\{10\},\mathrm{hex}} = \sqrt{3}a/2$. The corresponding q-vector then equals $q_{\{10\},\mathrm{hex}} = 2\pi/d_{\{10\},\mathrm{hex}} = 4\pi/(\sqrt{3}a)$. Comparing the square and hexagonal lattices, the q-vector relationship for the first diffraction is different by a term $2/\sqrt{3}$. In general the position of any GISAXS reflection in the horizontal scattering direction $\mathrm{q_y}$ with miller indices $\{h, k\}$ for a square lattice is equal to $q_{\{\mathrm{h,k}\},\mathrm{sq}} = \frac{2\pi}{a}\sqrt{h^2 + k^2}$, while for an 2-D hexagonal lattice it equals

$$q_{\{\mathrm{h,k}\},\mathrm{hex}} = \frac{4\pi}{\sqrt{3}\,a}\sqrt{h^2 + k^2 + hk}.$$

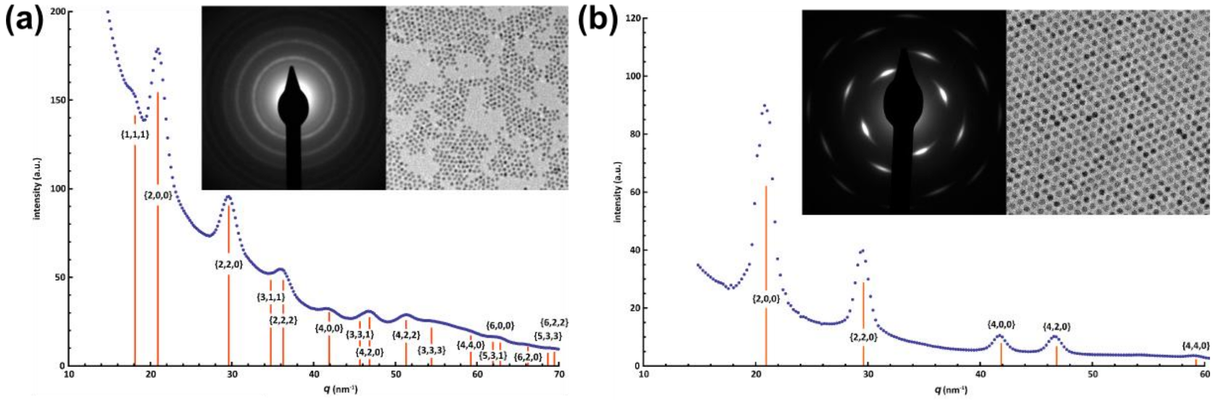

Figure S4: Azimuthally integrated electron diffraction patterns. The insets are the same images as **(a)** Fig. 1a and **(b)** Fig. 1g from the main text. Orange bars denote the positions of the atomic diffraction from PbSe (PDF card #00-006-0354). **(a)** All atomic reflections are visible, which indicates that the particles are not aligned with respect to the electron beam. **(b)** Only atomic reflections for nanocrystals with their <100> direction perpendicular to the substrate are observed.

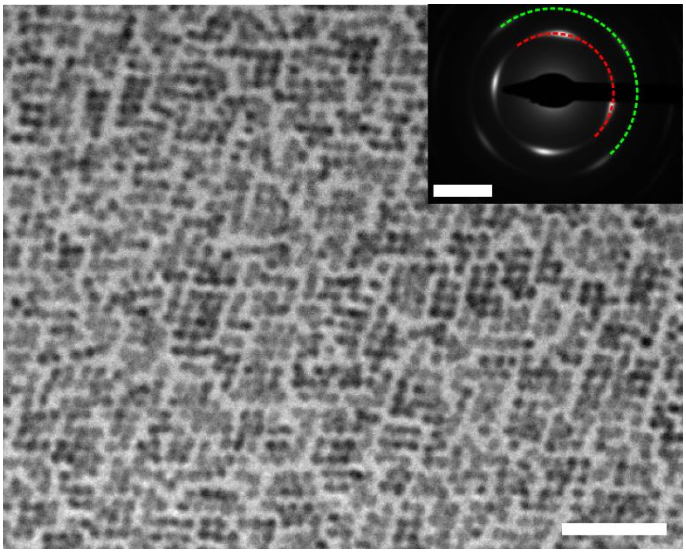

Figure S5: Characteristic TEM image of the sample scooped from the surface used in the in-situ experiments shown in Fig. 2 of the main text. Note the resemblance to Fig. 2(g). The micrograph shows that the NCs have assembled into a square superlattice. The NCs are atomically attached only in relatively small separate patches of 10-30 NCs, which could explain the peak broadening and absence of higher order diffraction rods in the GISAXS patterns. The electron diffraction pattern shows diffraction arcs, indicating atomic alignment of the particles. The coloured rings index the diffraction spots: red = {200} and green = {220}. Scalebars denote 50 nm in the TEM image and 20 nm^{-1} in the diffraction pattern. We should remark here that the formation of rather small domains that are atomically aligned has to do with the conditions under which in-situ measurements are done. Under better controlled conditions µm-large atomically coherent domains are observed (see e.g. figures S8).

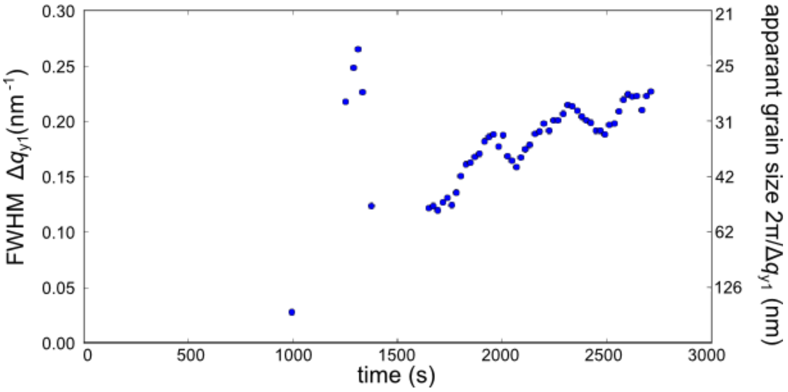

Figure S6: Analysis of the peak width of the first diffraction rod in the horizontal scattering direction Δq_{y1} during the GISAXS experiments shown in Fig. 2 of the main text. The grain size is calculated as $2\pi/\Delta q_{y1,}$,which corresponds to the Scherrer equation with K=1 if you realize that $\Delta q = 4\pi/\lambda \cos(\theta) \Delta(2\theta)/2$. To reduce X-ray beam damage on the sample we scanned the sample perpendicular to the incoming X-ray beam over an area of 4 mm. The peak widths are likely to come from superlattice grains on the sample with slightly different sizes.

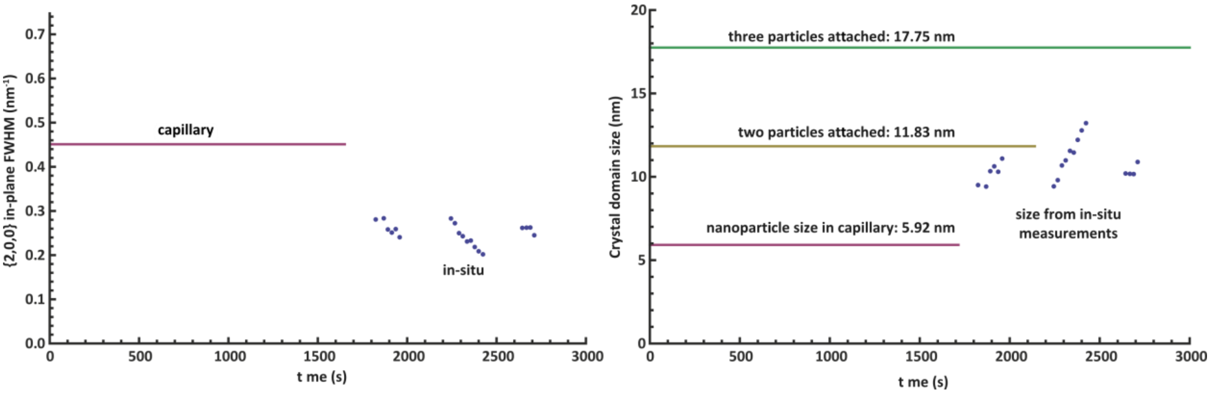

Fig S7: Evolution of the peakwidth of the horizontal {200} atomic reflection over time. Due to the large amount of experimental data, bad fits of the intensity profile were rejected from further analysis. **(a)** FWHM of the in-plane atomic {200} reflection over time. The purple line indicates the FWHM of the {200} diffraction of NCs dispersed in toluene, measured in a capillary. **(b)** The crystalline size is calculated as 2π/Δq , which corresponds to the Scherrer equation with K=1 if you realize that Δq = 4π/λ cos(θ) Δ(2θ)/2.

The crystalline size (5.92 nm) is in good agreement with the particle size obtained from TEM (5.7±0.6 nm). The blue dots represent the FWHM of the same atomic reflection during the in-situ experiments.

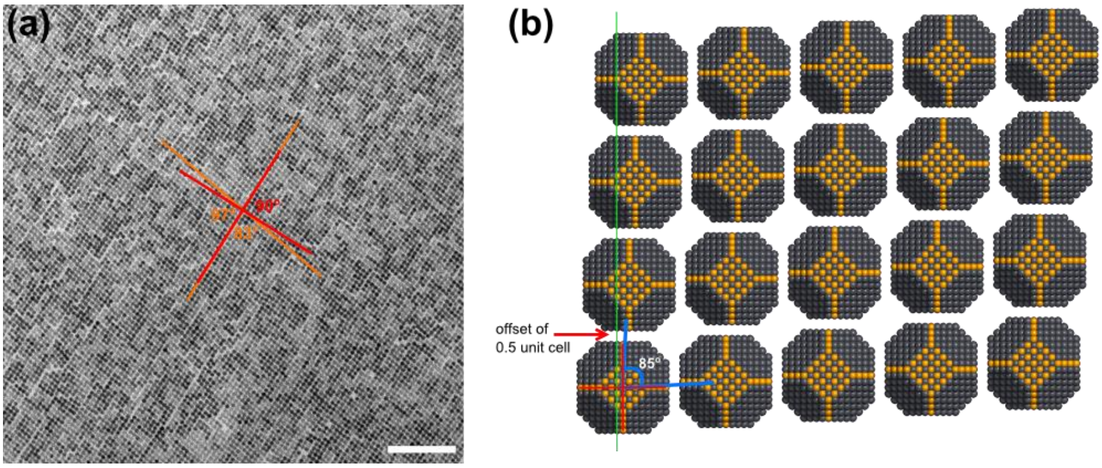

Figure S8: Discussion on the bond-angles in the final square superlattices. Due to the crystal structure of the individual PbSe nanocrystals, a shift of 0.5 unit cells in the two lateral directions is required to result in Pb-to-Se binding. The resulting bond angles would then be slightly larger or slightly smaller than 90°. **(a)** TEM image of a superlattice, where the deviation of the bond angles (83°/97°) with a perfect square lattice (90°) is clearly seen over longer distances. **(b)** Models of the PbSe nanocrystals in a square superlattice, where in both lateral directions the particles are shifted by half a unit cell. The scale bar in the TEM image equals 100 nm.

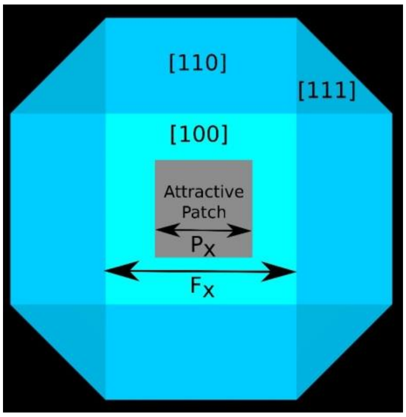

Figure S9: Model of the cantellated nanocube used in our NVT simulations. Different facets are indicated along with the attractive patch on the [100] facets. Dimension of the patch P_x and the [100] facet F_x are also indicated.

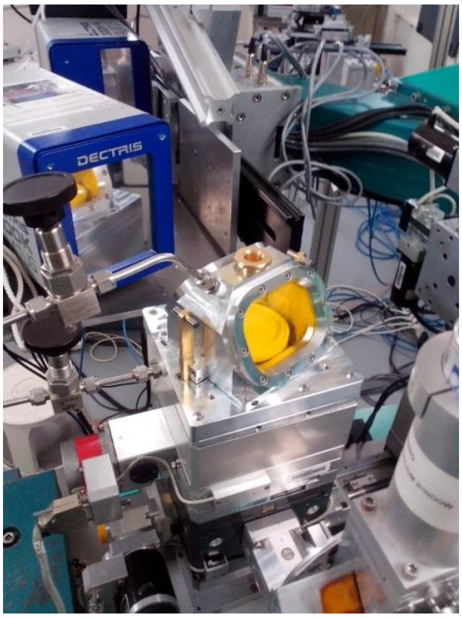

Figure S10: Photograph of the home-built liquid cell and setup used for the in-situ GISAXS/WAXS experiments at ID10 of the European Synchrotron Radiation Facility. The energy of the incident X-ray beam was set at 10.0 keV, below the Pb and Se absorption edges to minimize beam damage. We optimized the grazing angle to 0.3° for the best signal-to-noise ratio on both GIWAXS and GIWAXS detectors. As the PbSe NCs proved to be sensitive to beam damage, we scanned the sample position in between the measurement, back and forth over a distance of 4 mm (in 21 steps) in the direction perpendicular to the incident X-ray beam. In this way, the dose of X-ray photons on each position of the sample was minimized. Each frame was recorded with a 10 s integration time, after which the position of the sample was changed. After each sequence of 21 positions, we returned to the starting position and repeated the procedure.

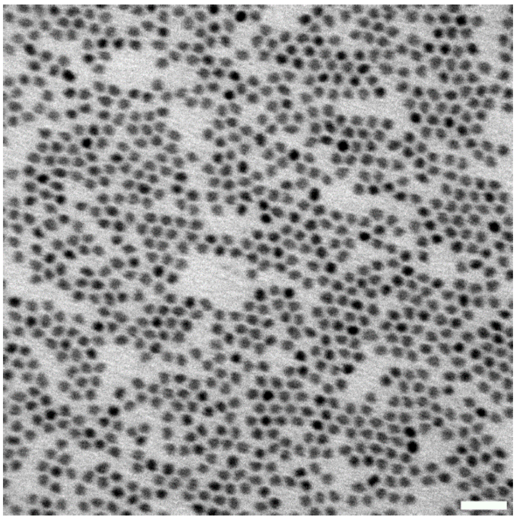

Figure S11: TEM image of the as-synthesized PbSe nanocrystals, with a diameter of 5.7±0.6 nm.

Supplementary methods 1: calculation of the X-ray penetration depth

The incident X-ray energy of 10 keV corresponds to a wavelength λ_0 = 0.124 nm and a wavevector of magnitude $k_0 = 2\pi/\lambda_0 =$ 50.7 nm^{-1} in air. For our experiments we used a grazing angle of incidence of 0.3°, slightly larger than the critical angle for total external reflection of bulk PbSe. Since the refractive index of any material is negative at X-ray frequencies ($n = 1 - \delta + i\beta$), the wavevector inside the sample $k = nk_0$ is smaller than in air. Upon transmission of the beam into the sample, the wavevector component parallel to the air–sample interface $k_{||} = k_0\cos(\alpha_i)$ is conserved. The wavevector component perpendicular to the sample is

$$k_z = \sqrt{k^2 - k_{||}^2} = k_0\sqrt{n^2 - \cos^2(\alpha_i)}$$

Since n is complex, k_z is complex. The imaginary part of k_z describes how quickly the X-ray intensity decays when going deeper into the sample. The penetration depth d, defined as the depth at which the X-ray intensity is lower by a factor e than at the interface, is given by

$$d = \frac{1}{2\,\mathrm{Im}(k_z)}$$

	δ	β
PbSe	1.292x10^{-5}	8.430x10^{-7}
Toluene	1.964x10^{-6}	1.750x10^{-9}
Ethylene glycol	2.539x10^{-6}	4.188x10^{-9}

Supplementary table S1: Values of the real (δ) and imaginary (β) part of the refractive-index decrement at 10keV for the materials used in these experiments. δ and β define refraction and absorption in a material accordingly.

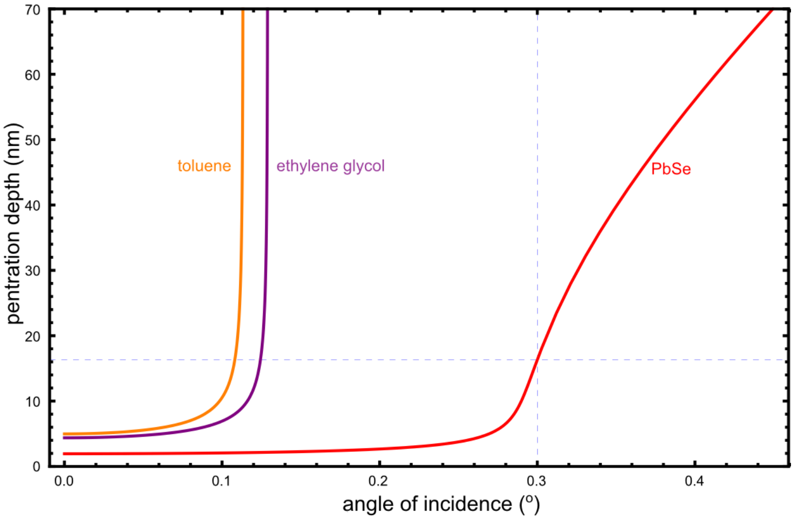

Figure S12: Calculation of the X-ray penetration depth as a function of incident angle. The red, purple and orange lines depict the penetration depths as function of incident angle for PbSe, ethylene glycol and toluene respectively. The blue dashed lines show the incident angle of the experiments (0.3°) and the corresponding penetration depth for PbSe (16.3 nm). Working at the critical angle of either toluene or ethylene glycol would result in a minute penetration of the X-ray photons into the PbSe superstructure.

Supplementary methods 2: computer aided image analysis

To determine the bond-angles, average NC-NC distances and surface density, we employed computer aided image analysis. The code used was written in the Python scientific programming language, with the addition of the numpy, matplotlib, scipy and opencv libraries.

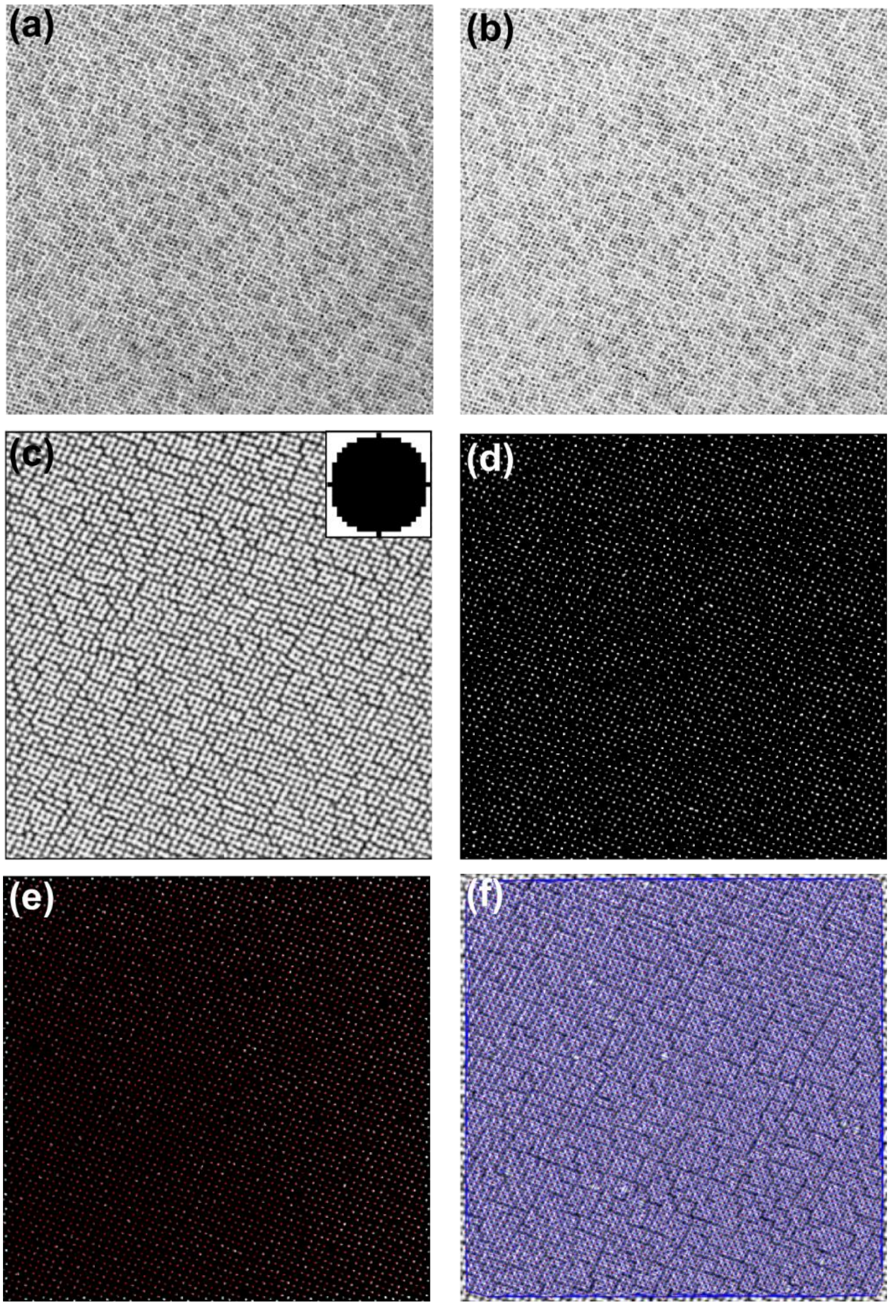

Figure S13: Schematic overview of the computer aided image analysis as performed in Python. **(a)** A TEM image is loaded into the program. **(b)** The TEM image is low-pass filtered with a 2D Gaussian ($\sigma <$ 0.6 nm) to remove ‘salt-and-pepper’ noise. **(c)** A spherical template of a dark particle on a white background is created and the cross correlation (CC) of the template with each pixel on the filtered image is calculated and averaged over multiple sizes of the spherical template. **(d)** The CC image is binarized and the centers of mass (COM) of the segments are determined. **(e)** COMs within 15 pixels of the image edge (red spots) are discarded to avoid edge artefacts. **(f)** On the remaining COMs a Delaunay triangulation was performed (blue mesh over the image).

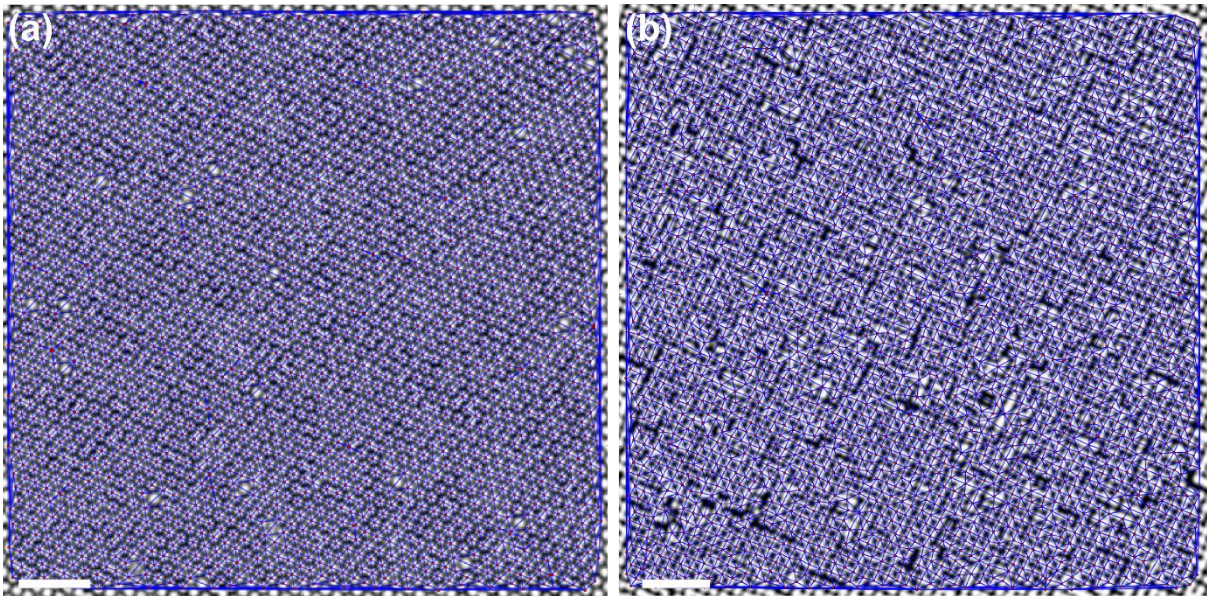

Figure S14: Computer aided image analysis on the TEM images. **(a)** The pseudo-hexagonal phase and **(b)**, the square phase. The red dots indicate the centers of mass, the blue mesh is the Delaunay triangulation over these centers of mass.

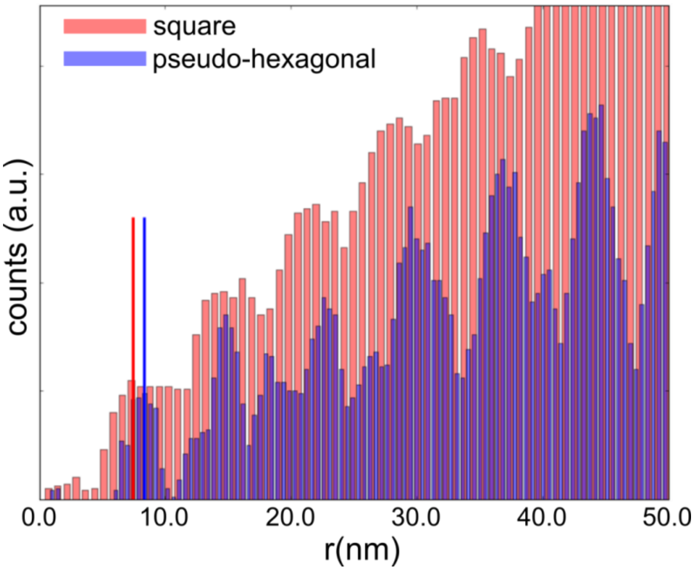

Figure S15: Radial distances obtained from the detected centers of mass for the PH phase (blue) and square phase (red). The blue and red vertical lines indicate the average NN distances for the PH and square phases respectively.

First, the centers-of-mass (COMs) of the PbSe NCs are automatically recognized using the procedure outlined in Figure S13. Next, from the COMs and the Delaunay triangulation the inter-particle distances and bond angles are determined. Furthermore from the surface area of the convex hull of the triangulation and the number of COMs, the number of particles per unit surface was determined.

From the histogram of the radial distances, the pair distribution function was extracted:

$$g(r) = \frac{\#\ \text{particles at distance } r}{2\pi r \cdot \mathrm{d}r \cdot \rho \cdot N}$$

Where g(r) is the pair distribution function, dr is the thickness of the circular shell at distance r, ρ is the average density of particles per unit surface and N the total number of detected particles.

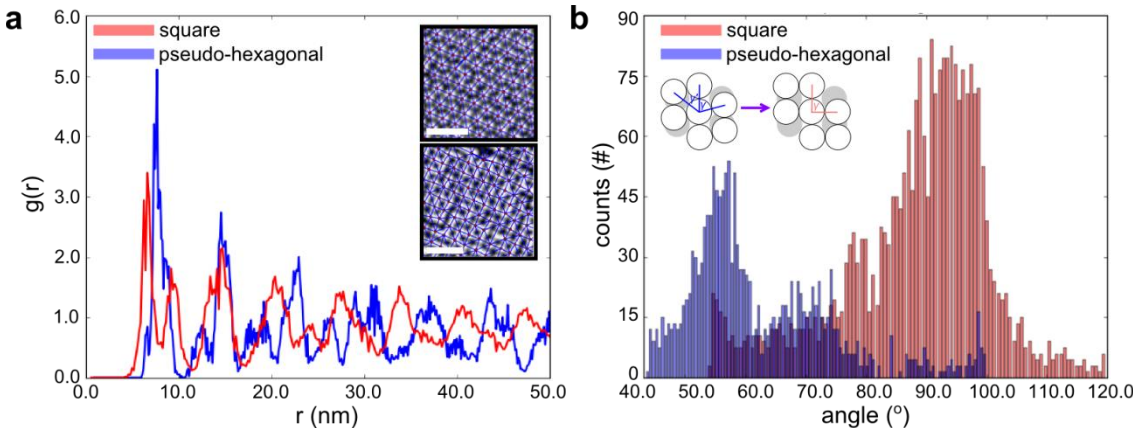

Figure S16: Image analysis on the PH and square phase TEM images. (a) *Pair distribution function obtained from the detected centers of mass of the PH phase (blue) and square phase (red). The large number of oscillations is a signature of extended positional order in the superlattice. The insets show the detected particles with the Delaunay triangulation mesh for the PH (top) and square (bottom) phase.* ***(b)*** *Bond angles of the superlattice in the PH (blue) and square phases (red). The inset shows a schematic of the two phases displayed on top of a perfect hexagonal crystal (grey dots). Scale bars in the TEM inset are 25 nm.*

To further analyze the intermediate phases occurring in the oriented-attachment process, we performed computer aided image analysis on the real-space TEM images of Fig. 1(g) and 1(k). Fig. 3(a) shows the pair distribution function of the NC–NC distances extracted for the pseudo-hexagonal (blue) and the square (red) phase. The nearest-neighbor distances decreases from 8.3±0.3 nm for the PH phase to 7.4±0.3 nm for the square phase (see Fig. S15). The contraction calculated from TEM images (11%) is smaller than that obtained from GISAXS (17%), as we could not isolate the pure hexagonal phase ex-situ. The bond angles of the superlattice are determined from the Delaunay triangulation, as shown in Fig. S16(b). The appearance of the 55° and 70° angles in the PH phase (blue bars) combined with the 2:1 peak intensity ratio are indicative for the deviation from a perfect hexagonal lattice. The square phase (red bars) has bond angles close to 90° (see Fig. S8).

The code for the automated particle detection is available online at:
http://www.filedropper.com/imageanalysisbrightfieldtem

or by emailing to j.j.geuchies@uu.nl.

Supplementary methods 3: modeling of GISAXS patterns for hexagonal, rhombic and square superlattices

We model scattering by the NC superlattice following a method [1,2] within the quasi-kinematic approximation. The NCs are modeled as spheres of radius *R*, for which the form factor is

$$P(q,R) = \left(3\frac{\sin(qR) - qR\cos(qR)}{(qR)^3}\right)^2$$

where $q = \sqrt{q_{||}^2 + q_z^2}$ is the total scattering vector, $q_{||}$ is the in-plane component, and q_z the out-of-plane component.

The structure factor of the 2-D crystal as a function of bond angle is calculated from the direct-space unit cell vectors. The resulting reciprocal lattice vectors $\boldsymbol{b_1}$ and $\boldsymbol{b_2}$ are used to calculate the reciprocal lattice. The diffraction condition is met for any scattering vector $\boldsymbol{q}$ that matches a reciprocal lattice vector $\boldsymbol{G}$. The total pattern (up to some value of *q*) is therefore obtained by summing over a range of *h* and *k* values:

$$S(q_{||}) = \sum_{h=-3}^{3}\sum_{k=-3}^{3} L(q_{||}, h\boldsymbol{b}_1 + k\boldsymbol{b}_2)$$

where

$$L(q_{||},\boldsymbol{G}) = \frac{\left(2\pi|q_{||}|\right)^{-1}}{\left[1+\Gamma^{-1}(q_{||} - |\boldsymbol{G}|)\right]^2}$$

is the Lorentzian line shape of each individual diffraction, with peak width Γ and centered at $|\boldsymbol{G}|$.

The effect of reflections on the liquid–gas interface is described by a Vineyard factor as:

$$V(q_z) = \begin{Bmatrix} 0 & \text{for } q_z < k_0\sin\alpha_i \\ \left|\dfrac{2\,k_{fz}}{k_{fz} + \sqrt{k_{fz}^2 + (k_0\sin\alpha_c)^2 + iv}}\right|^2 & \text{for } q_z \geq k_0\sin\alpha_i \end{Bmatrix}$$

Here $k_0 = 2\pi/\lambda$, $k_{fz} = q_z - k_0\sin(\alpha_i)$, α_c is the critical angle of the interface, α_i the angle of incidence, and $v = \beta/\delta$, where β and δ describe the refractive index of the sample $n = 1 - \delta + i\beta$. Since v is in the order of magnitude of 10^{-2}-10^{-3} for X-rays, we neglected this term in the simulations.

The total scattered intensity is then calculated as:

$$I(\boldsymbol{q}) = P(q,R)\,S\left(q_{||}\right)V(q_z)$$

It should be noted that the complete scattering pattern could be predicted in greater detail, including multiple scattering events, using the distorted-wave Born approximation, which goes however beyond the scope of this work.

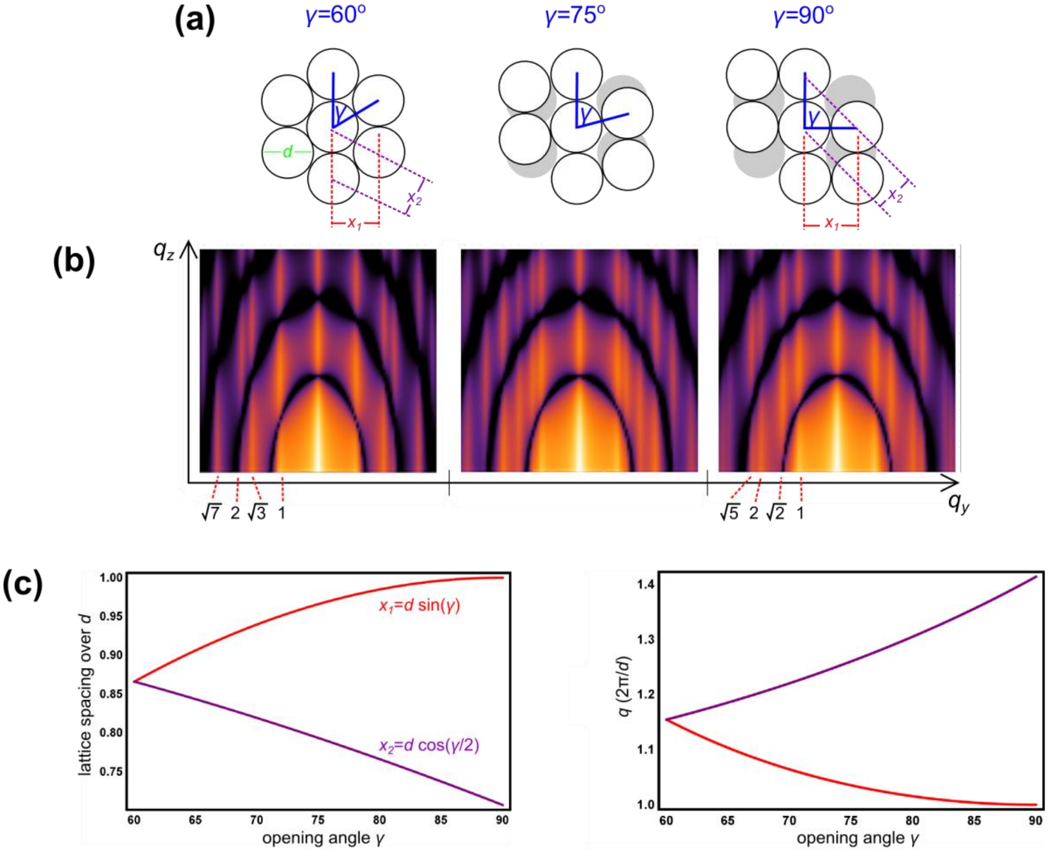

Figure S17: Simulated GISAXS pattern as function of bond angles. (a) The three models which were calculated: a 2-D hexagonal crystal, a 2-D crystal with a bond angle of 75° and a 2-D square crystal. The lattice planes that are equivalent in the hexagonal crystal (x_1 and x_2) break their degeneracy when the bond angle is changed from 60° to 90°. Here, *d* equals the diameter of the spheres. **(b)** Calculated GISAXS patterns for the corresponding 2-D crystals. Note how all diffraction rods split when the opening angle is 75°. Also note that for the 2-D square crystal the first higher order diffraction rod (indicated with $\sqrt{2}$) coincides precisely with the first form-factor minimum at low values of q_z. **(c)** The change of the relative lattice spacings x_1 and x_2 over *d*, when going from the 2-D hexagonal crystal to the 2-D square crystal in direct space (left) and reciprocal space (right). Note how the degeneracy is lifted when the bond angle differs from 60°.

Supplementary methods 4: calculation of the position of the atomic reflections on the GIWAXS detector

We want to obtain the peak position of the atomic diffraction when the nanocrystals are aligned not only in the 2θ-direction but also in the φ-direction. We put the center of the sample surface at the origin of our coordinate system, the z-axis to be along the X-ray beam, the x-axis perpendicular to the sample surface and the y-axis perpendicular to both. The *x*-component of the scattered wavevector written in polar coordinates is:

$$k_{\mathrm{out},x} = |\boldsymbol{k}_{\mathrm{in}}| \sin\theta_{\mathrm{p}} \cos\varphi$$

The component θ_{p} is the polar angle the scattered beam makes with respect to the z-axis, which is equal to the Bragg angle (2θ), and can be calculated with the Bragg equation. The magnitude of the incoming X-ray wavevector, $|\boldsymbol{k}_{\mathrm{in}}|$, is given by 2π/λ. The x-component of the outgoing wavevector, $k_{\mathrm{out},x}$, can be calculated by addition of a reciprocal lattice vector to $k_{\mathrm{in},x}$

$$k_{\mathrm{out},x} = k_{\mathrm{in},x} + g_{\mathrm{h}}$$

As the nanocrystals are oriented on the surface, they are only free to rotate around the x-axis. The x-component of the reciprocal lattice vector, g_{h}, is unaffected by rotations around the x-axis and therefore remains *2πh/a*. In which *h* is the Miller index the x-direction and *a* is the lattice spacing of rock salt PbSe. As this crystal structure possesses cubic symmetry (space group $Fm\overline{3}m$), the *h*, *k* and *l* components of the reciprocal lattice are interchangeable. The x-component of the incoming X-ray wavevector, $k_{\mathrm{in},x}$, is equal to zero, as we have chosen our z-axis to be parallel to the X-ray beam. If we now plug in the resulting $k_{\mathrm{out},x}$ back in our first equation, we have a complete description of the θ and φ values for every possible reflection *{h,k,l}*;

$$\theta = \sin^{-1}\left(\frac{\lambda\sqrt{h^2+k^2+l^2}}{2a}\right)$$

$$\varphi = \cos^{-1}\left(\frac{h\cdot\lambda}{2\pi\cdot\sin 2\theta}\right)$$

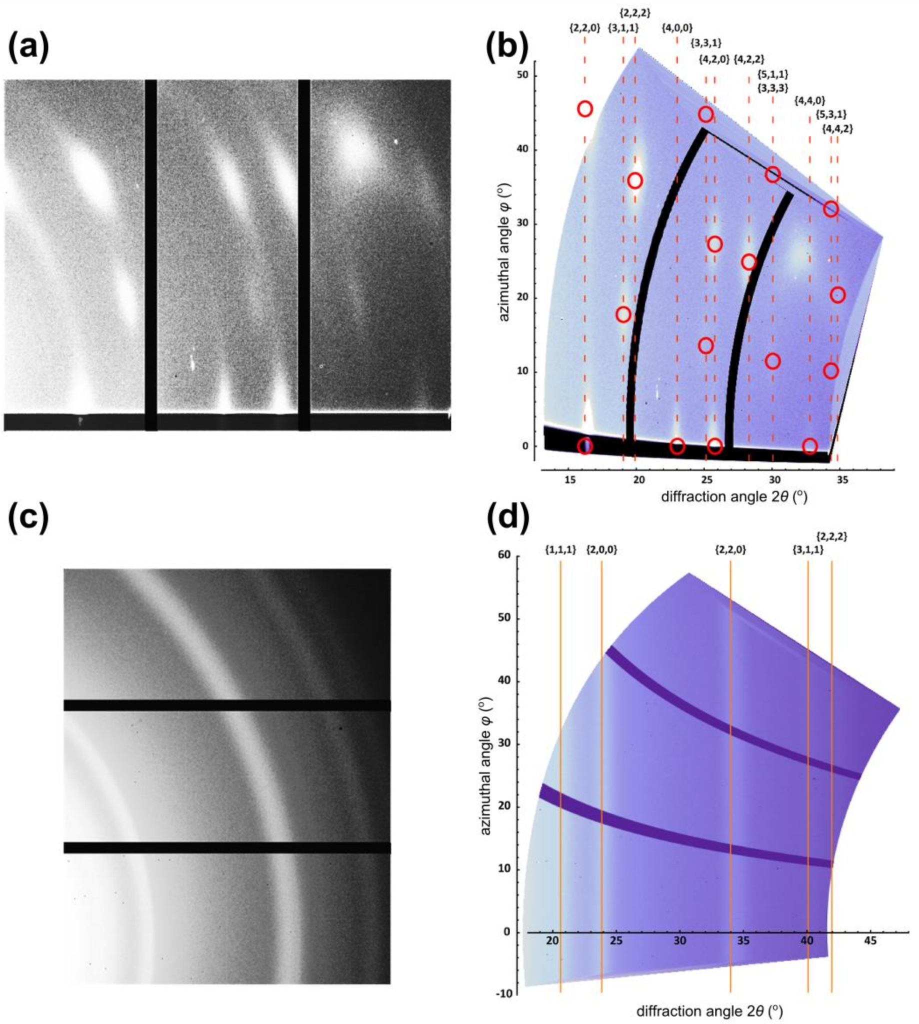

Figure S18: GIWAXS parametrization and data analysis. **(a)** Atomically aligned NCs on top of a Si-(100) substrate with their [100] axis perpendicular to the surface, giving rise to diffraction spots on the GIWAXS detector. **(b)** Same image, after coordinate transformation from pixel values to 2θ and ϕ values. The red dots are the positions of the expected atomic reflections. The only unlabeled diffraction peak at $(2\theta, \varphi) = (32^o, 28^o)$ corresponds to a Si reflection, the sample substrate. These GIWAXS patterns were recorded during initial experiments at an X-ray energy of 20.7 keV. **(c)** GIWAXS of the PbSe NCs in solution. These are identical particles to those used for the in-situ experiments in the main text. **(d)** Transformed GIWAXS image, showing the position of the diffraction rings. Experiments recorded with the same experimental parameters as the in-situ experiments.

Supplementary methods 5: **peakwidth of atomically aligned, but not attached, nanocrystals**

The diffraction signal is as a first order approximation equal to the squared Fourier Transform of the electron density profile. We approximate the NC superlattice here as a one-dimensional chain of connected crystal and we consider the horizontal [100] direction. The lattice vector in the [100] direction equals 6Å. Each NC consists out of *N* (100) planes in the horizontal direction, for the NCs used in the experiments *N*= 8-10. The length from the start of a nanocrystal to the next nanocrystal is *L* and the total chain consists out of *M* of these repeating units in the positive *x* direction.

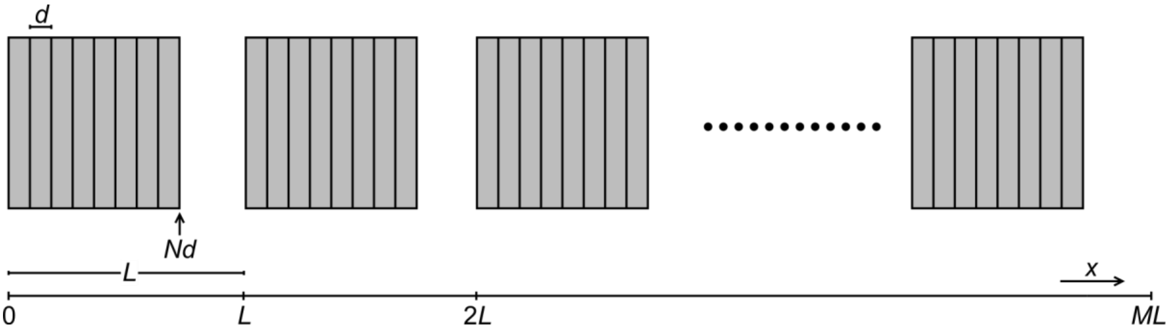

Figure S19: nanocrystal model used to approximate the peak widths. Each nanocrystal has a *N* lattice planes with a lattice spacing *d*. The length from the start of the NC to its neighbour equals *L*.

The Fourier Transform of this chain of *separated*, *but aligned*, nanocrystals is given by

$$F(q) = \int_{0}^{ML} \rho(x) e^{-iqx} dx$$

which can be split into a sum of repetitions of the first segment

$$F(q) = \sum_{j=0}^{M-1} \int_{0+jL}^{L+jL} \rho(x) e^{-iqx} dx$$

This summation can be expanded as

$$F(q) = \int_{0}^{L} \rho(x) e^{-iqx} dx + \int_{L}^{2L} \rho(x) e^{-iqx} dx + \int_{2L}^{3L} \rho(x) e^{-iqx} dx + \ldots + \int_{M-1}^{ML} \rho(x) e^{-iqx} dx$$

$$= \int_{0}^{L} \rho(x) e^{-iqx} dx + \int_{0}^{L} \rho(x) e^{-iq(x+L)} dx + \int_{0}^{L} \rho(x) e^{-iq(x+2L)} dx \ldots$$

$$= \sum_{j=0}^{M-1} e^{-iqLj} \int_{0}^{L} \rho(x) e^{-iqx} dx$$

The summation above has a general solution, given by

$$S_N = \sum_{n=0}^{N} a_0\, q^n = a_0 \frac{q^{N+1} - 1}{q - 1}$$

Hence the summation outside of the integral is given by

$$\sum_{j=0}^{M-1} e^{-iqLj} = \frac{e^{-iqML}-1}{e^{-iqL}-1}$$

The integral itself, which runs over a single segment of length L can be evaluated in an equivalent manner:

$$\int_0^L \rho(x)e^{-iqx}dx = \int_0^{Nd} \rho(x)e^{-iqx}dx + \int_{Nd}^{L} \rho(x)e^{-iqx}dx$$

The second integral is equal to zero as there is no electron density in between the nanocrystals. The second integral is evaluated equivalently to the summation over all nanocrystals and gives

$$\int_0^{Nd} \rho(x)e^{-iqx}dx = \frac{e^{-iqNd}-1}{e^{-iqd}-1}\int_0^{d} \rho(x)e^{-iqx}dx = \frac{e^{-iqNd}-1}{e^{-iqd}-1} S_n$$

Where we treat the Fourier Transform of the electron density in between the lattice planes, S_n, as a constant.

The intensity is measured as $|F(q)|^2$ and can now be approximated by:

$$I(q) \propto \frac{\sin^2\left(\frac{qML}{2}\right)}{\sin^2\left(\frac{qL}{2}\right)} \frac{\sin^2\left(\frac{qNd}{2}\right)}{\sin^2\left(\frac{qd}{2}\right)}$$

We assume a perfect positioning of the nanocrystals in the above derivation. This situation is not realistic, but can be improved by assuming a Gaussian distribution of the nanocrystal positions:

$$I(q) \propto \int_0^{\infty} e^{-\frac{1}{2}\left(\frac{L-L_0}{\sigma L}\right)^2} \frac{\sin^2\left(\frac{qML}{2}\right)}{\sin^2\left(\frac{qL}{2}\right)} \frac{\sin^2\left(\frac{qNd}{2}\right)}{\sin^2\left(\frac{qd}{2}\right)} dL$$

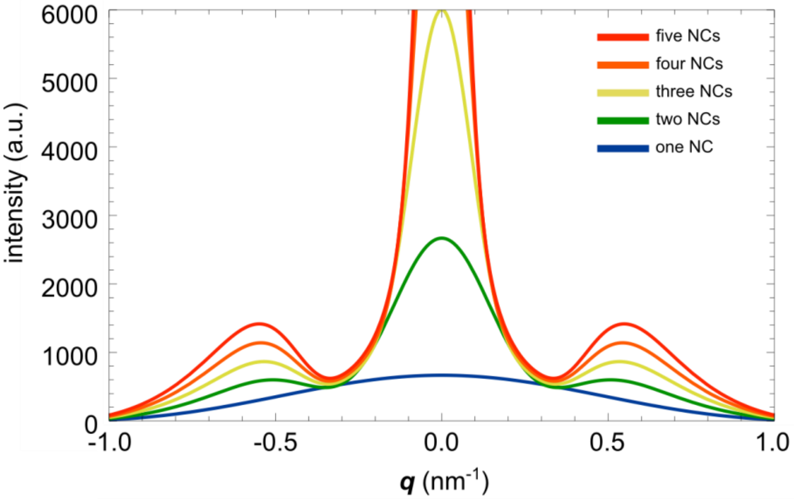

Figure S20: peak width of aligned but not connected nanocrystal as a function of increasing number of attached nanocrystals. Plotted are the scattering curves using *d* = 0.6 nm, *N* = 9 (the product *N*d* gives a realistic nanocrystal size), L_0=1.53**N***d*. We used *σL* = 0.4*L_0.

It can be seen that the peak width decreases slightly upon increasing the number of aligned particles, due to the variations in the nanocrystal positions, assumed to mimic the in-situ experimental conditions.

The approximation used above is only accounting for a variation in the particle positions. When we assume further disorder by considering the NC rotational freedom along all three Cartesian axes, the peak width of the diffracted signals will decrease even less.

Upon perfect alignment of the particles (no rotational misalignment, no distribution in the particle positions) the peak width decreases. However, we consider the latter situation to be unrealistic and do assign the decrease in atomic peak width to be due to particle attachment.

Supplementary methods 6: azimuthal and radial peakwidths in electron diffraction

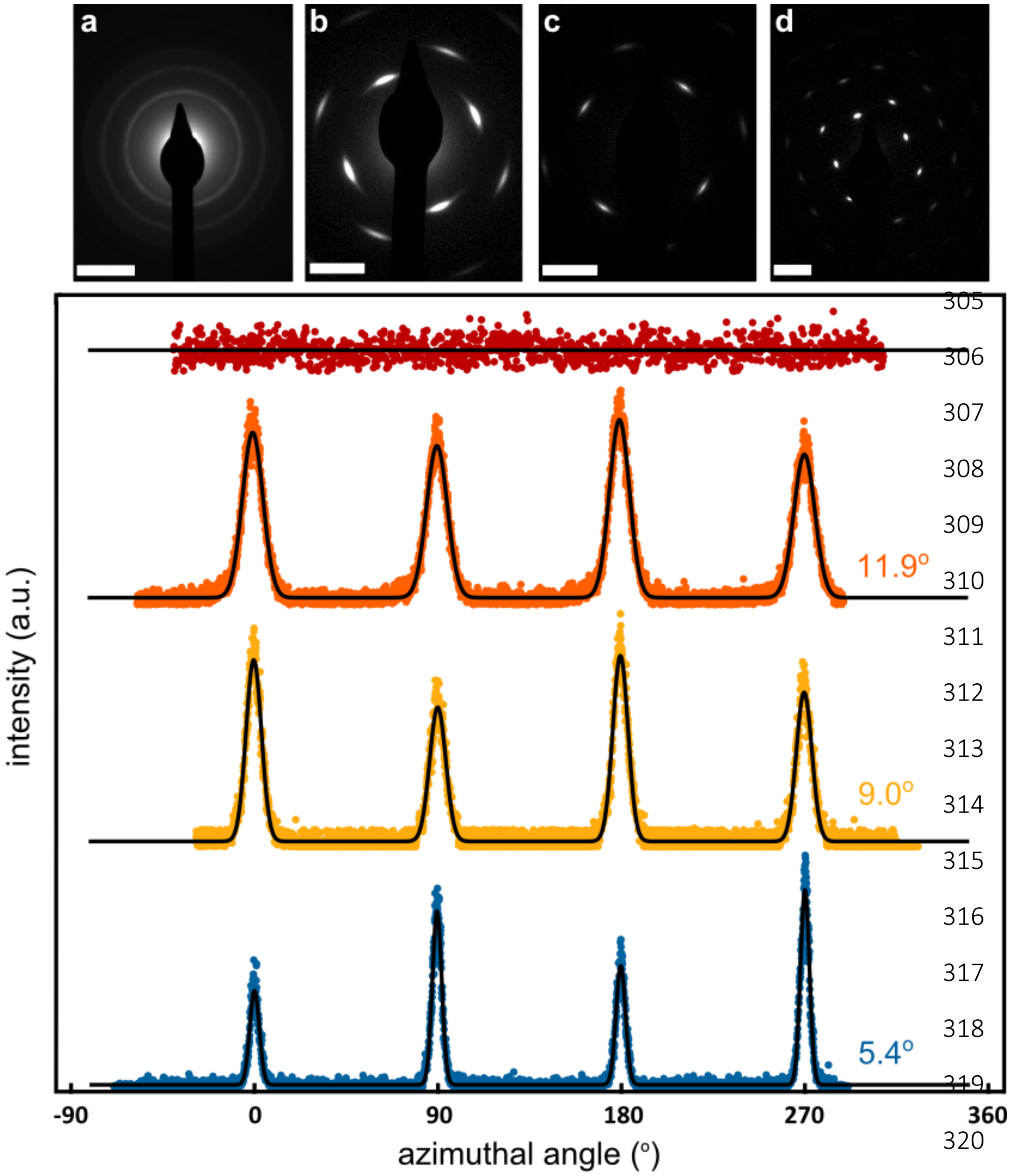

Figure S21: azimuthal peak widths of the electron diffraction patterns during the self-assembly process. ED patterns and azimuthal azimuthal traces over the {400} reflection show a decrease in peak width, which indicates the loss of in-plane rotational freedom of the nanocrystals during the self-assembly process.

Azimuthal traces over the {400} reflections from the electron diffraction patterns in the main text are presented in the figure above. Going from completely disordered NCs (Fig. S20(a)) to the square superlattice with attached nanocrystals (Fig. S20(d)) the peak widths of the {400} reflections decrease, showing that the nanocrystals have less in-plane rotational freedom with respect to each other. We should remark here that the data should not be interpreted in a quantitative way, as instrumental broadening is not taken into account here.

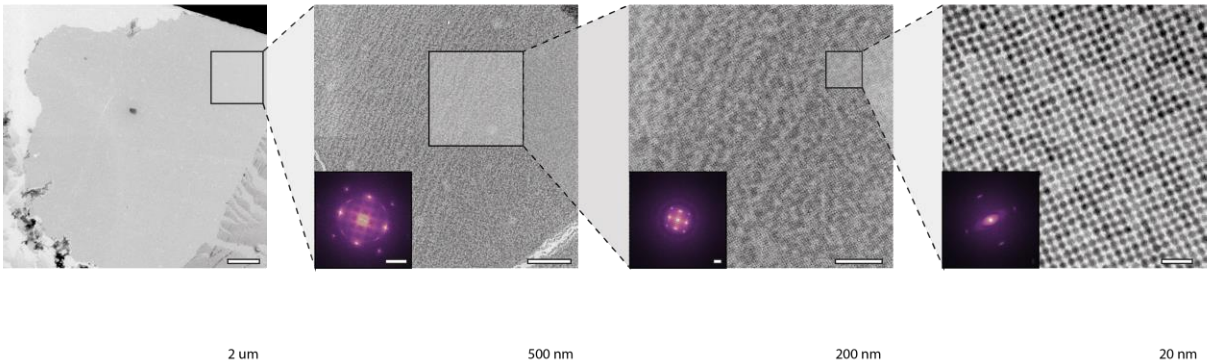

Figure S22: Conservation of nanocrystalline order on mesoscopic length scales. *From left to right consecutive zoomed in TEM images are displayed, which show a very long-range periodicity. Even though the atomic coherency throughout the complete lattice is conserved over several nanocrystals, this does not perturb the long-range nano-crystalline order. From the widths of the {100}-superlattice reflections in the Fourier transforms we obtain nanocrystal coherence lengths for the superlattice of 39.3 nm, 34.3 nm and 35.9 nm from left to right. Scale bars from left to right images are 2µm, 500nm, 200nm and 20 nm respectively and 1 nm^{-1} for all Fourier transform insets.*

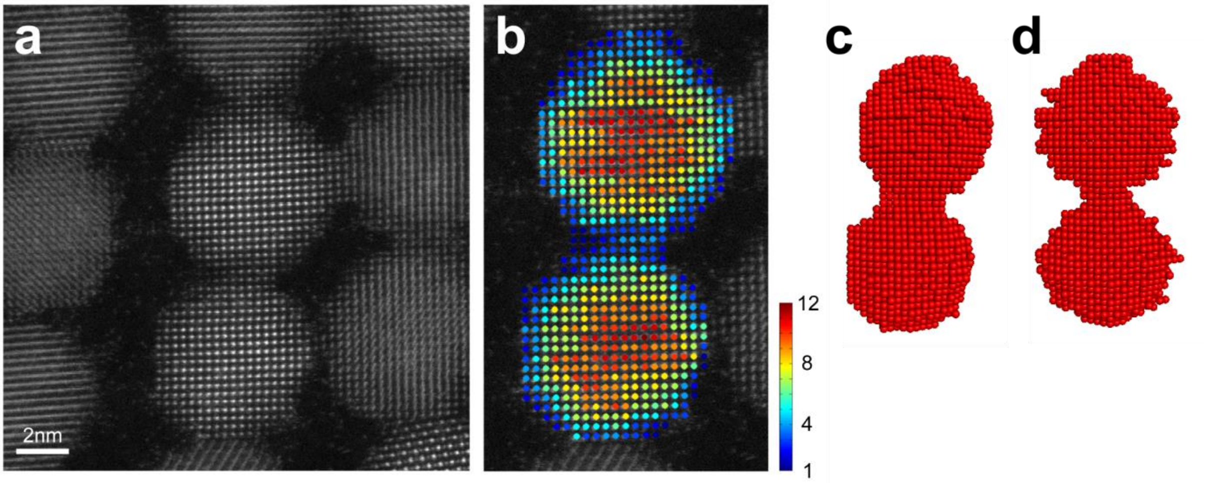

Figure S23: HAADF-STEM and atom counting reconstruction on attached NCs. (a) *HAADF-STEM image of NCs attached in a square superlattice. The atomic periodicity is continued from a given NC to its neighbors. Slight misorientations can also be observed.* ***(b)*** *Results from the atom counting procedure, using (a) as an input image. The color bar represents the number of detected atoms in each vertical column.* ***(c)*** *Top-view and* ***(d)*** *side-view of the reconstructed atomic model.*

Supplementary methods 7: Coulomb and Van Der Waals interactions between nanocrystals

We model the interaction between two PbSe nanocrystal cubes (consisting out of 3375 atoms) through electrostatic and Van Der Waals interactions. We assume an ionic model for rocksalt PbSe. For the calculation of the Coulomb potential between two nanocrystals, we sum the Coulomb potentials of each ion in nanocrystal 1 in interaction with all ions in nanocrystal '2'. This is performed for a given relative position of nanocrystal 1 with respect to nanocrystal 2. Hence the Coulomb interaction is given by:

$$V_{coulomb} = \frac{1}{4\pi\varepsilon_0}\sum_{i}^{N_i}\sum_{j}^{N_j}\frac{q_i q_j}{r_{ij}}$$

Where With ε_0 the vacuum permittivity, q_i and q_j the charges on atom 1 (located in nanocrystal 1) and atom 2 (located in nanocrystal 2). The double sum runs over all pairs of atoms in nanocrystal *i* and nanocrystal *j*.

The Van Der Waals interaction is calculated as spontaneous dipole-induced dipole (otherwise known as London or dispersion interactions);

$$V_{VdW} = -\frac{3}{2}\sum_{i}^{N_i}\sum_{j}^{N_j}\frac{I_i I_j}{I_i + I_j}\frac{\alpha_i \alpha_j}{r_{ij}^6}$$

With I_i and I_j the first ionization energies of atom 1 and 2 and α_i and α_j the polarizabilities of atom 1 and 2. Again both atoms are located in nanocrystal 1 and nanocrystal 2 respectively. For Pb the first ionization energy equals 715,6 kJ/mol and the polarizability equals 6.8 Å^3. For Pb the first ionization energy equals 715,6 kJ/mol and the polarizability equals 6.8 Å^3.

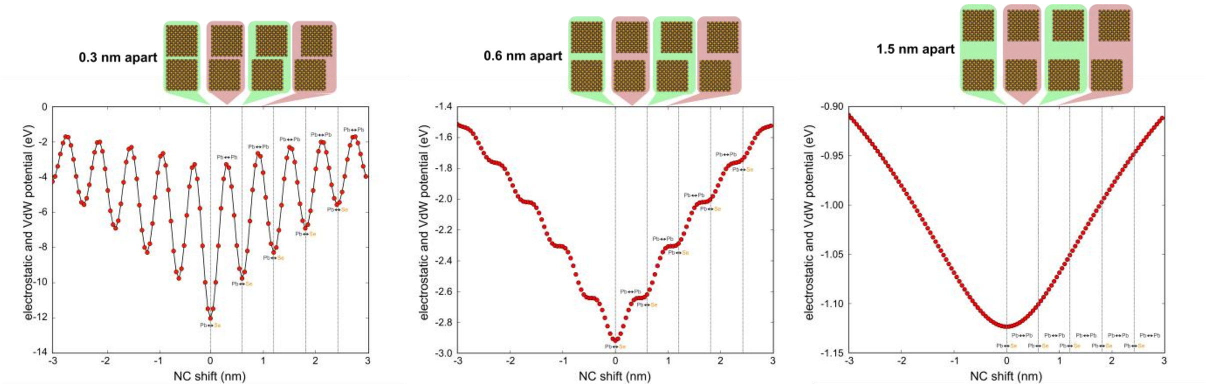

Figure S24: The interaction between two nanocubes of PbSe upon lateral displacement. *The left, middle and right images shows the interaction potential when the nanocrystals are 0.3 nm, 0.6 nm and 1.5 nm apart respectively.*

When we start from the ideal situation, i.e. the nanocrystals are exactly opposing each other and Pb ions face Se ions, the energy is strongly increased upon moving the nanocrystals half a unit cell along the x-axis because of direct short range repulsions.

At a distance of 0.3 nm (left image in Fig. S23), the oscillations of the interaction potential have the same period as the unit cell and are quite pronounced. When we increase the distance between the nanocrystals to 0.6 nm, these oscillations are still visible, indicating preferential orientation of the atomic lattices favoring Pb-to-Se alignment. The 0.6 nm distance approaches realistic experimental conditions. When we further increase the distance to 1.5 nm, the oscillations disappear, but there is a general potential minimum when the nanocrystal [100] facets have maximum overlap. Such a potential leads an attractive driving force between the nanocrystals for maximum {100} to{100} facet overlap, be it with half a unit cell mismatch to maximize the interactions between ions of opposite charge.

In the simulations of the hexagonal to square phase transitions, the above potential is mimicked by attractive patches centered on the vertical {100} facets of each nanocrystal, representing a similar driving force for maximal facet-to-facet overlap as following from the atomistic calculations.

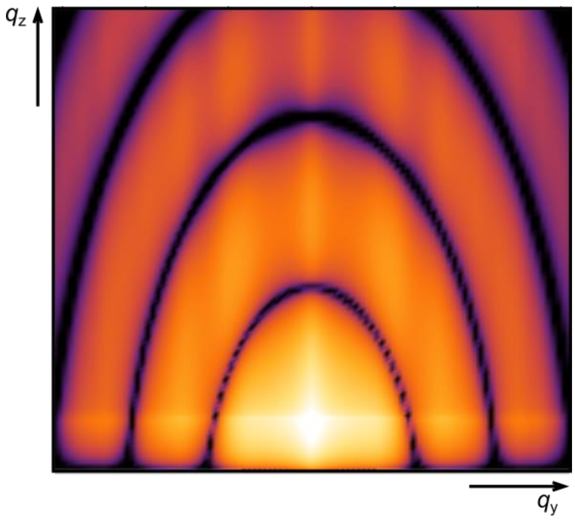

Figure S25: Expected GISAXS pattern for a slightly oblique square lattice. Calculated for a slightly distorted square lattice with a bond angle of 83^{o} and additional broadening due to the small superlattice grain size. Note the agreement with the experimental GISAXS patterns obtained during the in-situ experiments.

References

1. Heitsch, A. T., Patel, R. N., Goodfellow, B. W., Smilgies, D.-M. & Korgel, B. A. GISAXS Characterization of Order in Hexagonal Monolayers of FePt Nanocrystals. *J. Phys. Chem. C* **114,** 14427–14432 (2010).

2. Smilgies, D.-M., Heitsch, A. T. & Korgel, B. A. Stacking of hexagonal nanocrystal layers during Langmuir-Blodgett deposition. *J. Phys. Chem. B* **116,** 6017–6026 (2012).